Enzymatic Micromotors as a Mobile Photosensitizer Platform for Highly Efficient On-Chip Targeted Antibacteria Photodynamic Therapy

Dandan Xu, Chao Zhou, Chen Zhan, Yong Wang, Yongqiang You, Xi Pan, Jiapu Jiao, Ran Zhang, Zhijun Dong, Wei Wang, and Xing Ma*

Photodynamic therapy (PDT) functions when the light-excited photosensitizers transfer energy to oxygen molecules ($^3O_2$) to produce cytotoxic singlet oxygen ($^1O_2$) that can effectively kill cells or bacteria. However, the PDT efficacy is often reduced by the limited availability of $^3O_2$ surrounding the photosensitizer and extremely short diffusion range of the photoactivated $^1O_2$. Herein, an enzymatic micromotor based on hollow mesoporous SiO_2 ($mSiO_2$) microspheres is constructed as a mobile and highly efficient photosensitizer platform. Carboxylated magnetic nanoparticles are connected with both hollow spheres and 5,10,15,20-tetrakis(4-aminophenyl)porphyrin molecules through covalent linkage between amino and carboxylic groups within a one-step reaction. Due to the intrinsic asymmetry of the $mSiO_2$ spheres, the micromotors can be propelled by ionic diffusiophoresis induced by the enzymatic decomposition of urea. Via numerical simulation, the self-propulsion mechanism is clarified and the movement direction is identified. By virtue of active self-propulsion, the current system can overcome the long-standing shortcomings of PDT and significantly enhance the PDT efficacy by improving the accessibility of the photosensitizer to $^3O_2$ and enlarging the diffusing range of $^1O_2$. Therefore, by proposing a new solution to the bottleneck problems of PDT, this work provides insightful perspectives to the biomedical application of multifunctional micro/nanomotors.

D. Xu, Dr. C. Zhan, Y. Wang, Y. You, X. Pan,
J. Jiao, R. Zhang, Prof. X. Ma
State Key Laboratory of Advanced
Welding and Joining
Flexible Printed Electronic Technology Center, and School
of Materials Science and Engineering
Harbin Institute of Technology (Shenzhen)
Shenzhen 518055, China
E-mail: maxing@hit.edu.cn
C. Zhou, Prof. W. Wang
School of Materials Science and Engineering
Harbin Institute of Technology (Shenzhen)
Shenzhen 518055, China
Dr. Z. Dong
Shenzhen Institute of Information Technology
Shenzhen 518172, China

The ORCID identification number(s) for the author(s) of this article can be found under https://doi.org/10.1002/adfm.201807727.

1. Introduction

Photodynamic therapy (PDT) is a repeatable, controllable, and site-specific therapeutic technique which has been widely investigated in fundamental research and practically employed in clinical medicine.[1] The principle of PDT process relies on the energy transfered from light-excited photosensitizer to the surrounding oxygen molecules ($^3O_2$) to generate cytotoxic/reactive oxidant species (ROS) of singlet oxygen ($^1O_2$) for effective cancer cells or bacteria killing.[2] Although PDT has achieved significant progress in both research and clinical application, several physical limitations have greatly impeded the therapeutic efficacy of the PDT process, including the availability of $^3O_2$ molecules nearby photosensitizers[3] and short diffusion range of $^1O_2$,[4] as well as poor water solubility of most highly efficient photosensitizer molecules.[5] Nanotechnology, in particular mesoporous nanomaterial based nanocarriers such as mesoporous silica[6] and metal–organic framework (MOF),[7,8] has been employed to solve the problem of poor water solubility of photosensitizers, which helps to prevent the self-aggregation induced photodynamic quenching. Additionally, researchers have endeavored to increase oxygen generation and/or diminish oxygen dependence by in situ reaction on nanocarriers to overcome hypoxia for efficient PDT.[9] However, most of the current photosensitizer platforms are still essentially passive nanocarriers and thus the generated $^1O_2$ can only approach the targeted organism by their own free diffusion.[10] As is reported, the lifetime of $^1O_2$ is very short (below 0.01 ms) and the root mean square diffusion distance traveled by a $^1O_2$ molecule is only within 100–200 nm in water.[11] Therefore, one good solution for more effective PDT is to enlarge the diffusion range of the generated $^1O_2$ which has seldom been explored yet.

Micro/nanomotors (MNMs), or synthetic microswimmers, can convert diverse energy sources into mechanical motion in a controllable manner, which have been functionalized for a variety of applications.[12,13] Recent breakthroughs have been reported on utilizing functionalized MNMs for biomedical

applications, including targeted drug delivery, mini-surgery, biochemical sensing, and diagnostics.[13–15] In particular, MNMs as active carriers with the capability of cargo loading and controllable motion have great potentials for effective delivery of different types of cargos.[15] So far, researchers have also explored stimuli-responsive materials,[16–19] biomimetic materials,[20–22] and micro-organisms functionalized with nanomaterials[23] as MNMs to precisely transport cargos of drugs,[16,20,23,24] proteins,[18,22,25] and genes[19] in vitro and/or in vivo. Compared with traditional passive delivery, MNMs can perform tasks such as controlled navigation, rapid transportation, and active delivery of payloads to disease sites, and thus have paved way for on demand biomedical cargo transportation.[15] Inspired by these achievements, we envision that self-propelled MNMs can serve as a mobile photosensitizer platform to improve the availability of $^3O_2$ as well as the diffusion range of $^1O_2$, which can consequently achieve highly efficient PDT process.

Hereby, we developed an enzymatic magnetic hollow mesoporous SiO_2 micromotor loaded with 5,10,15,20-tetrakis(4-aminophenyl)porphyrin (TAPP, a highly efficient but hydrophobic photosensitizer) (MHSTU), as a mobile photosensitizer platform (**Figure 1**a). TAPP was loaded onto the magnetic nanoparticles which were anchored on the external surfaces of the hollow $mSiO_2$ microspheres. Due to chemical bonding between carboxylic groups of magnetic nanoparticles (Fe_3O_4—COOH) and amine groups of TAPP, TAPP molecules were separated in monomeric state[26] to avoid the quenching of PDT effect caused by self-aggregation in physiological condition.[27] Instead of constructing Janus structures by conventional strategy of depositing new material onto a monolayer of particles, the as-prepared hollow microspheres formed by one-step reaction in bulk synthesis have intrinsic asymmetric property contributed by the holes on the surfaces of the hollow $mSiO_2$ spheres (HS). The MHSTU can be propelled by the urease-triggered biocatalytic reaction of urea on
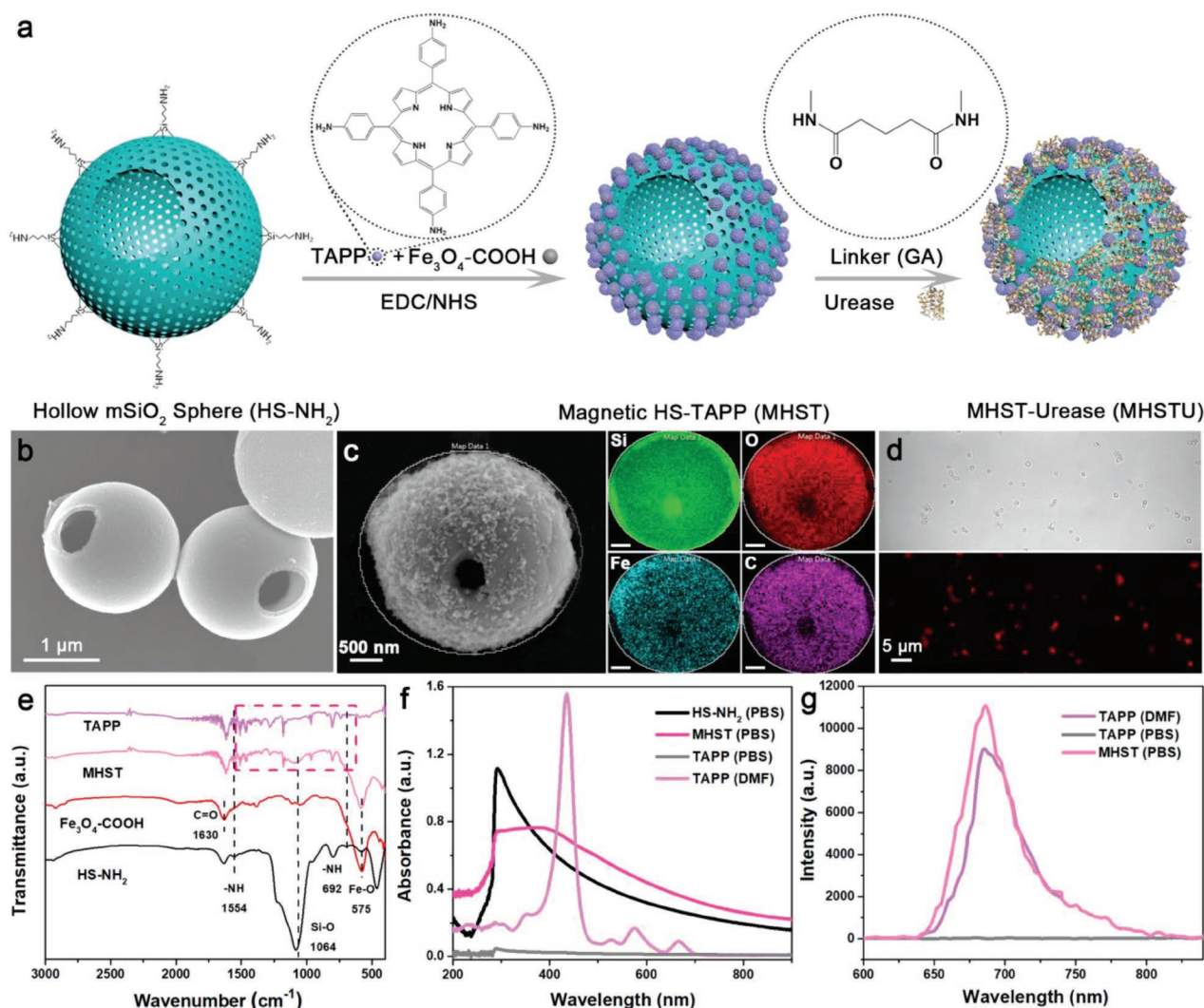
Figure 1. a) Schematic illustration of the fabrication of urea-propelled magnetic micromotors (MHSTU), SEM images of b) HS-NH$_2$ and c) MHST with corresponding elemental mapping by EDS. d) Brightfield and fluorescent image of MSTU. e) FT-IR spectra of HS-NH$_2$, Fe$_3$O$_4$—COOH, MHST, and TAPP. f) UV–vis spectra of HS-NH$_2$, MHST, TAPP suspended in PBS, and TAPP dissolved in DMF. g) Fluorescence spectra of MHST and TAPP suspended in PBS, and TAPP dissolved in DMF.

its asymmetric structure. The motors also possess magnetotaxis behavior for remotely targeted transportation by external magnetic field. The random motion of the urea-driven MHSTU can increase the $^1O_2$ generation rate by improving the accessibility to the $^3O_2$ molecules and also spread toxic $^1O_2$ molecules to a much larger area, resulting in enhanced photodynamic toxicity. We have demonstrated the antibacteria *Escherichia coli* (*E. coli*) PDT process via flow cytometry assay and fluorescence microscopy. Taken together, such a self-propelled platform could provide new perspectives to the functionalization and application of MNMs, as an example of the synergy between self-propulsion and biologically relevant functionalities of MNMs.

2. Result and Discussion

2.1. Fabrication and Characterization of the MHSTU

As is illustrated in Figure 1a, HS prefunctionalized with amine groups (HS-NH$_2$) was prepared by cocondensation method using polystyrene microparticles as templates according to our previously reported strategy.[28] The scanning electron microscope (SEM) images of polystyrene microparticles are given in Figure S1 in the Supporting Information, showing a diameter of 2.0 ± 0.2 µm (error bar indicates standard deviation, $N = 50$). The highly concentrated polystyrene templates are usually crowded with each other so that mSiO$_2$ only grows on the exposed surfaces of the templates. When the templates were removed, there turned out to be one hole or more on the surfaces of the HS-NH$_2$ spheres as shown in Figure S2 in the Supporting Information. The morphology of as-prepared HS-NH$_2$ was characterized by SEM (Figure 1b), where a hole with a diameter of about 400 nm was observed on the surface of the hollow spheres resulting in structural asymmetry for the motors. Fe$_3$O$_4$—COOH was also prepared according to a previous report with minor modifications.[29] Additional information including SEM image, X-ray diffraction (XRD) pattern, size distribution, and zeta potential of Fe$_3$O$_4$—COOH nanoparticles was provided in Figure S3 in the Supporting Information. Then, magnetic HS-NH$_2$ loaded with TAPP (MHST) was obtained by one-step surface chemistry process, where amino groups on both HS-NH$_2$ and TAPP reacted with carboxylic groups on Fe$_3$O$_4$—COOH by 1-ethyl-3-(3-dimethylaminopropyl)carbodiimide (EDC)/*N*-hydroxylsuccinimide (NHS) chemistry (Figure 1a). Next, the enzyme urease was bonded to the external surface of MHST by using glutaraldehyde (GA) as a linker, named as MHSTU.[28]

Figure 1c shows the SEM image of a typical MHST which evidences the presence of Fe$_3$O$_4$—COOH nanoparticles on the external surface of the hollow sphere. Corresponding elemental analysis by energy dispersive spectrometer (EDS) further confirms the surface modification of magnetic nanoparticles by the coexistence of multiple elements including Si, O, Fe, and C. We also took the optical image of MHST under the brightfield and fluorescent channel with blue light (480 ± 40 nm) excitation, which shows the hollow structure of the microspheres with red fluorescence emission contributed by the TAPP molecules, indicating the successful linkage of TAPP on the surface of MHST (Figure 1d). In addition, the fabrication process was traced by Fourier transform infrared (FT-IR) spectra of HS-NH$_2$,

Fe$_3$O$_4$—COOH, MHST, and TAPP. As is shown in Figure 1e, the peak at 1064 cm^{-1} can be assigned to Si—O bond from the silica shell.[30] Then, the peak at 575 cm^{-1} owing to the stretching of Fe—O[31] and the typical peaks of TAPP such as 805, 966, 1078, and 1508 cm^{-1}, were also identified in the spectrum of the MHST. Furthermore, the peak at 1630 cm^{-1} due to the C=O bond of the carboxylic groups of Fe$_3$O$_4$—COOH[29] and those at 1554 and 692 cm^{-1} aroused from the stretching of amino groups of HS-NH$_2$,[32] were all found in the FT-IR spectrum of the MHST. Given the evidences provided above, we can conclude that the MHST has been prepared as designed successfully.

We also investigated the optical properties of MHST. As shown in Figure 1f, TAPP in *N,N*-dimethylformamide (DMF) exhibits a strong characteristic absorption peak at about 435 nm, while that suspended in phosphate buffered saline (PBS) does not show any absorption peaks between 200 and 850 nm. The results indicate TAPP kept monomeric in DMF and the characteristic peak of TAPP in PBS disappeared because of the self-aggregation of hydrophobic TAPP molecules in aqueous condition.[27] Compared with the absorption spectrum of HS-NH$_2$, that of MHST shows an extra broad "shoulder" at about 435 nm, which was due to the presence of TAPP. Furthermore, the fluorescence spectrum of the MHST in PBS shows apparent characteristic emission peak at about 685 nm, the same as that of monomeric TAPP in DMF, which was not detected in that of TAPP suspended in PBS (Figure 1g). It is proven that TAPP on MHST is kept monomeric in PBS, which is crucial for further efficient photodynamic activity in aqueous condition.[7] The fluorescent property of MHST was also confirmed by the red color emission directly observed under fluorescent microscopy as shown in Figure 1d.

2.2. Motion Behavior of the Urea-Driven MHSTU

Janus structure has been widely explored for the fabrication of MNMs, in order to achieve geometric asymmetry and thus directional self-propulsion.[33] In the current case, taking advantage of the intrinsic asymmetric property contributed by the hole on the surface of the hollow mSiO$_2$ sphere formed by one-step chemical reaction, the MHSTU can achieve phoretic motion driven by enzymatic reaction (the conversion of urea by urease into NH$_3$ and CO$_2$) on its asymmetric structure. **Figure 2a** displays typical video snapshots of an MHSTU swimming in an aqueous solution containing 25 mmol L^{-1} urea (Video S1, Supporting Information). Under the phase contrast mode of the optical microscopy, it is observed that the urea-driven MHSTU motor was moving away from a clear "cavity" on the hollow sphere (see the inset images in Figure 2a), which suggests that the micromotor was moving away from the hole on the MHSTU sphere. The accordingly asymmetric structure of MHSTU and its movement propelled by the decomposition of urea are schematically illustrated in Figure 2b.

Janus microspheres asymmetrically functionalized with enzymes are known to self-propel in appropriate substrate solutions,[28] and diffusiophoresis is commonly invoked to explain such self-propulsion.[34] The presence of holes on the hollow mSiO$_2$ spheres naturally break the symmetry, yet how the enzymatic reactions lead to propulsion away from the hole
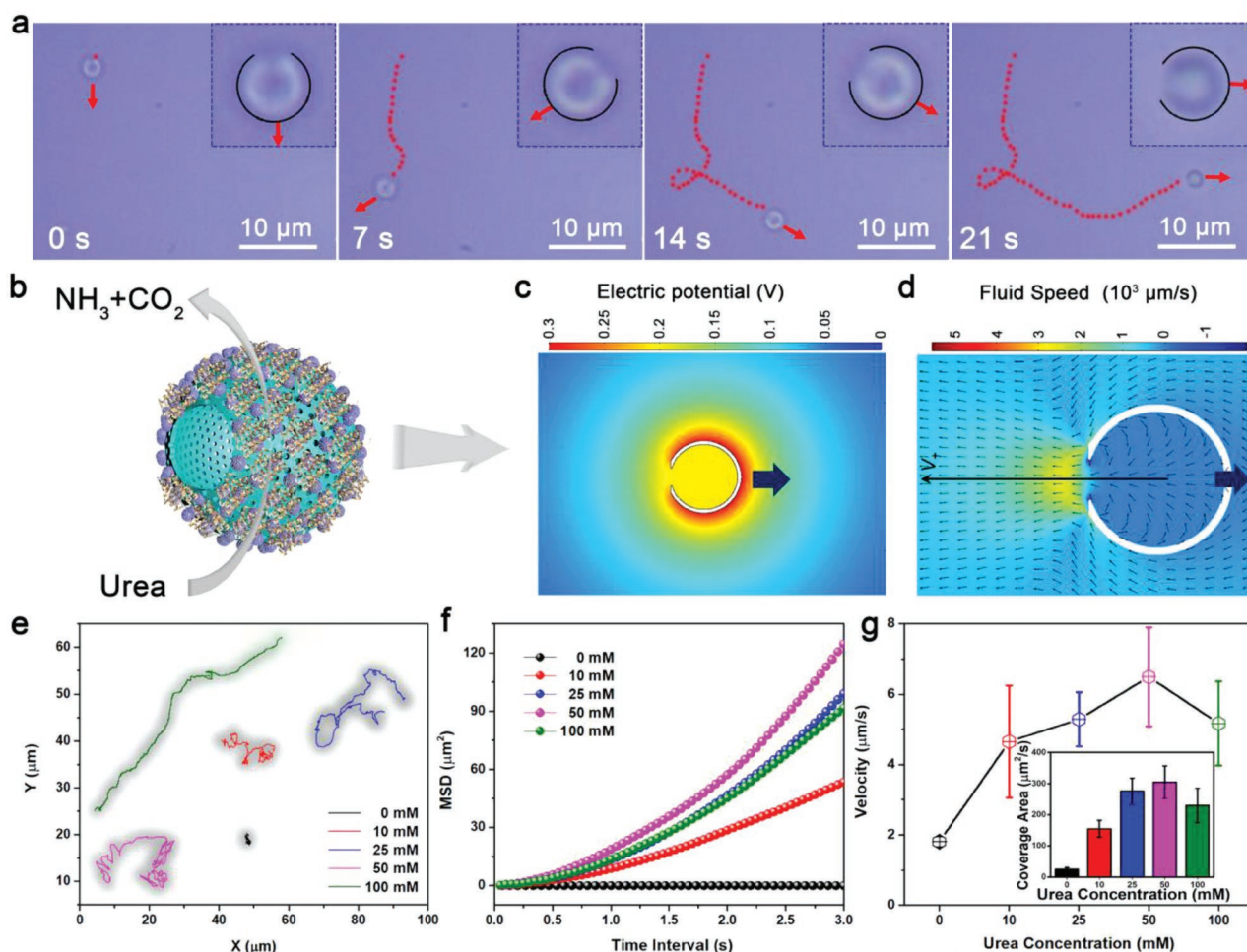
Figure 2. a) Video snapshots of a MHSTU swimming in 25 mmol L^{-1} urea solution toward the opposite direction of the hole of the MHSTU. b) Schematic illustration, c) the electrical potential distribution (color-code), and d) flow field (black-arrow) of MHSTU powered by urea. e) Typical tracking trajectories of MHSTU swimming in urea solution with different urea concentrations up to 15 s. f) Curves of mean-square-displacement (MSD) versus the time interval (Δt) with varied urea concentrations. g) Velocity and average coverage area (inset) of MHSTU swimming in urea solution with different urea concentrations up to 15 s. Error bars indicate standard deviation, $N = 15$.

is not intuitive. To understand this propulsion mechanism, we performed numerical modeling of an MHSTU particle that is uniformly covered with urease on the outer surface except for the region at the hole (modeling details are shown in the Experimental Section). In this model, we assume a uniform outward flux of NH_4^+ and OH^- ions, while ignore the effect of CO_2 and related ions due to the much lower solubility of CO_2 than NH_3. Since the diffusion of OH^- is much faster than NH_4^+ (5.27×10^{-9} vs 1.95×10^{-9} m^2 s^{-1}), therefore an electric field pointing outward is spontaneously established to maintain electroneutrality outside of the electrical double layers (in Figure 2c). The presence of a hole on the MHSTU surface distorts the electric field and induces an electro-osmotic flow around the negatively charged particle surface pointing toward the hole (Figure 2d). Thus, an MHSTU particle moves away from its hole. Based on this qualitative and simplified model, we explained the directionality of MHSTU motors powered by an ionic diffusiophoresis mechanism. In addition, simulation results suggest various factors that could affect the directionality and speed of the urea-driven MHSTU, including the

shape, size, number, and distribution of the hole, as well as the enzyme distribution on the surface of MHSTU,[35] which will be studied in conjunction with experiments in our future work.

Based on optical video recordings with a frame rate of about 30 fps, typical tracking trajectories of the urea-driven MHSTU at 0, 10, 25, 50, and 100 mmol L^{-1} urea are presented in Figure 2e. The results display that MHSTU at 0 mmol L^{-1} urea performed Brownian motion only, while those with the presence of urea exhibited active self-propulsion with increasing trajectories dependent on urea concentration. The typical video of MHSTU swimming in 25 mmol L^{-1} urea solution is provided in Video S1 in the Supporting Information. According to the extracted 2D coordinates (x, y) along the trajectories, we obtained the curves of mean-square-displacement (MSD) versus the time interval (Δt) with varied urea concentrations (Figure 2f).[35] In Figure 2f, parabolic MSD curves show increasing slope values in the linear range until the urea concentration is up to 50 mmol L^{-1}, suggesting a transition from Brownian diffusive motion to directional self-propulsion. We also calculated the velocity of the urea-driven MHSTU versus the urea concentration.

The velocity of the urea-driven MHSTU continues to increase with the increasing urea concentration at the beginning, and slightly drops when the urea concentration is 100 mmol L^{-1} (Figure 2g). It is suggested that the enzymatic activity is dependent on the fuel concentration for low urea concentrations, and starts to saturate at the concentration of 50 mmol L^{-1} when the velocity is about 6.49 μm s^{-1}. Afterward, the enzymatic activity is inhibited by the intrinsic inhibition of urea at high concentration, which probably due to the reported denaturing effect of urea on proteins or a competition between urea and water.[36] We also studied the movement behavior of enzymatic powered MHSTU in saline (NaCl) solution and found that the speed of the urea-driven MHSTU decreases with the increasing concentration of NaCl at the urea concentration of 25 mmol L^{-1} (Figure S4, Supporting Information), which supports the ionic diffusiophoresis mechanism proposed in our numerical model.

We hypothesize that with the increasing coverage area, this active photosensitizer platform is supposed to acquire more $^3O_2$ molecules and also spreads the in situ produced toxic $^1O_2$ molecules to a much larger area, which can greatly improve the PDT effect in comparison to passive photosensitizer carriers. To better evaluate the capabilities of acquiring $^3O_2$ and spreading $^1O_2$, we also calculated the "coverage area" of the urea-driven MHSTU within 15 s as shown by the shadow area in Figure 2e. The inset of Figure 2g shows the average coverage area of the urea-driven MHSTU versus the urea concentration, which demonstrates the similar variation trend to that of the velocity shown in Figure 2g. The coverage area of MHSTU powered by 25 mmol L^{-1} urea is about 275.67 μm^2 s^{-1} which is more than 10 times larger than that of passive MHSTU in water (25.43 μm^2 s^{-1}). Then, we chose the urea concentration of 25 mmol L^{-1} to propel MHSTU for the following PDT experiments, which can ensure excellent motion behaviors. In addition, the video of an MHSTU swimming in aqueous solution with 25 mmol L^{-1} urea under fluorescent mode observation shows red fluorescence emission (see Figure S5 and Video S2 in the Supporting Information), which ensures the photodynamic activity during its movement in the following investigation.

2.3. On-Chip Targeted Magnetotaxis Transportation of the Motors

Due to the surface attached magnetic nanoparticles, the micromotors are equipped with magnetic property which facilitates the precise manipulation of the micromotors. Hereby, we demonstrate the magnetotactic transportation of MHSTU for targeted PDT process as shown by the schematic illustration in **Figure 3**a. We utilized a self-built 2D magnetic control platform
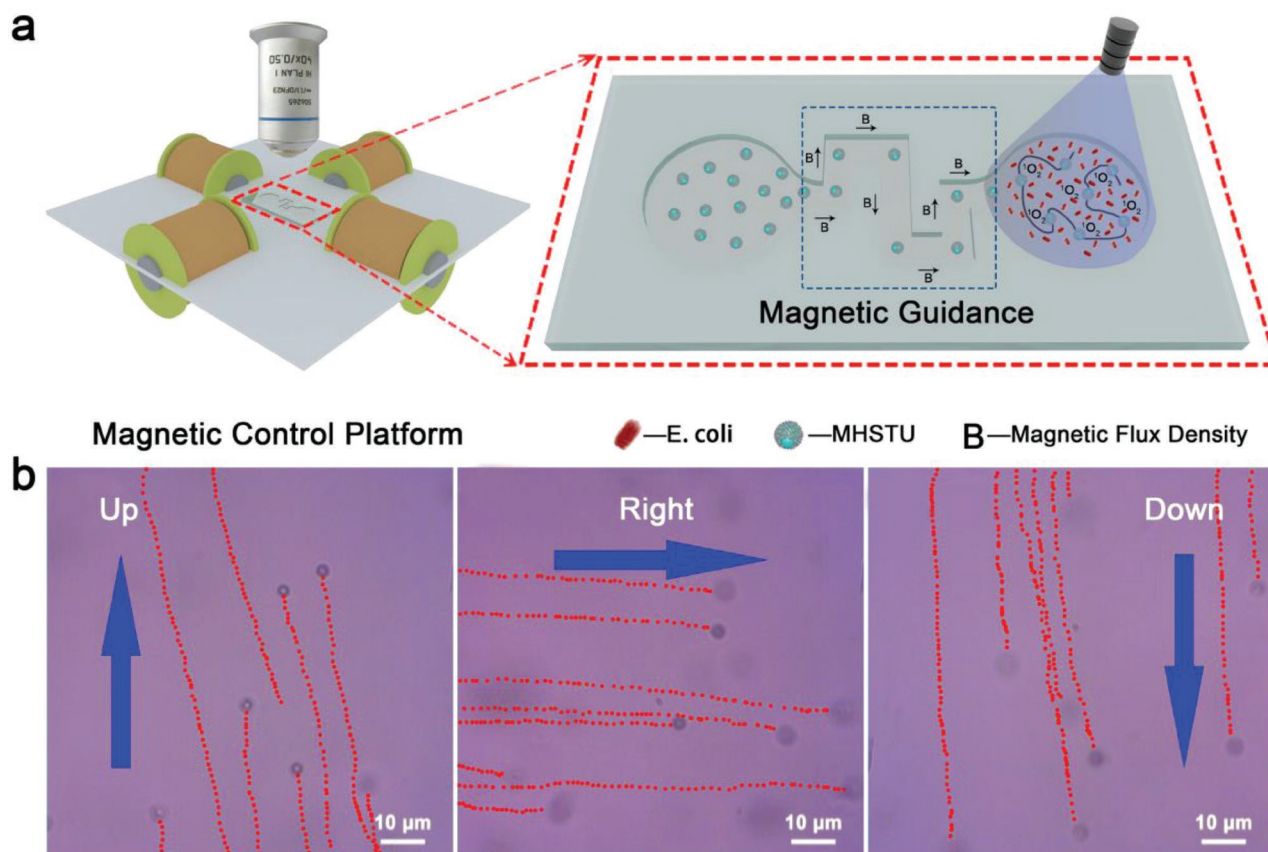
Figure 3. a) Schematic illustration of the self-built 2D magnetic control platform for on-chip magnetic guidance on MHSTU and the magnification of the movement condition of the MHSTU motors on the chip. B is a vector on behalf of the direction of the magnetic field. b) Video snapshots of the swarming movement of MHSTU guided by the external magnetic field.

at the current of 1.4 A and the voltage of 24 V to manipulate the MHSTU and transport a group of micromotors on a self-designed chip with two chambers connected with complex channels. The strength of the generated magnetic field was about 10 mT.

We carried out the controlled transportation of the MHSTU motors with magnetic taxis by generating a gradient magnetic field in required dimension (Video S3, Supporting Information).[37] The MHSTU motor can be attracted and moved in a straight line aligned with the direction of the applied gradient magnetic field (Figure S6, Supporting Information). Once we switched the direction of the magnetic field, the MHSTU motor altered its movement direction accordingly. Video S4 in the Supporting Information was recorded during the on-chip targeted transportation process at different channels of three directions, showing that the motors performed swarming movement in the same direction as demanded. In such a manner, by external magnetic field manipulation, we can accomplish transportation of the micromotors at will, passing through the on-chip channels to approach targeted chambers for further on-demand PDT task against bacteria (Figure 3b). Capable of controllable locomotion, this platform can deliver photosensitizers in a targeted way and provide the opportunity for precise localized biomedical treatment.

2.4. $^1O_2$ Generation Capacity Assessment

As illustrated in **Figure 4**a, MHSTU can induce the biocatalytic decomposition of urea for active movement, while the loaded TAPP molecules on MHSTU can be excited by light irradiation (450 nm) to generate cytotoxic $^1O_2$ molecules which are simultaneously spread around within the culture dish to kill *E. coli*. The $^1O_2$ generation capability of the MHSTU motor was assessed by using ABDA (9,10-anthracenediyl-bis-(methylene)dimalonic acid) as the $^1O_2$ trapped agent, and monitored by UV–vis absorption spectroscopy.[8] The absorbance of ABDA continuously decreased because part of ABDA molecules reacted with the generated $^1O_2$, which in turn reflects the amount of generated $^1O_2$ in solution. First, the solution containing MHSTU (1 mg mL^{-1}) and saturated ABDA was irradiated by 450 nm light (3.9 mW cm^{-2}) that can excite the TAPP to generate $^1O_2$. The obtained UV–vis absorption peak between 300 and 450 nm of the solution decreases continuously shown in Figure S7 in the Supporting Information, which indicates that ABDA was oxidized by the generated $^1O_2$. What's more, we systematically compared the capability of $^1O_2$ generation by tracing the variation trend of the absorbance peak values at 378 nm of ABDA for different control groups shown in Figure 4b. For the several negative control groups without any light irradiation, including blank sample (red), treated with urea (purple), MHSTU (navy), and both MHSTU and urea (olive), the absorbance of ABDA remains almost unchanged. Under blue light irradiation, the absorbance of ABDA with both MHSTU and urea fueled MHSTU decreases continuously within 20 min. The absorbance of ABDA with urea fueled MHSTU drops faster than that with MHSTU only. It is reasoned that the urea-driven MHSTU as a mobile photosensitizer platform can access to more $^3O_2$ molecules, resulting in more than 20% higher productivity of $^1O_2$ than the motionless MHSTU.

Additionally, videos showing *E. coli* in deionized (DI) water, *E. coli* in 25 mmol L^{-1} urea solution, MHSTU and *E. coli* in DI water, as well as MHSTU and *E. coli* in 25 mmol L^{-1} urea solution are provided in Video S5 in the Supporting Information. The video shows that *E. coli* in DI water, *E. coli* in 25 mmol L^{-1} urea solution, as well as MHSTU and *E. coli* in DI water all performed Brownian motion, whose movement area were confined to a certain range indicated by black circles in
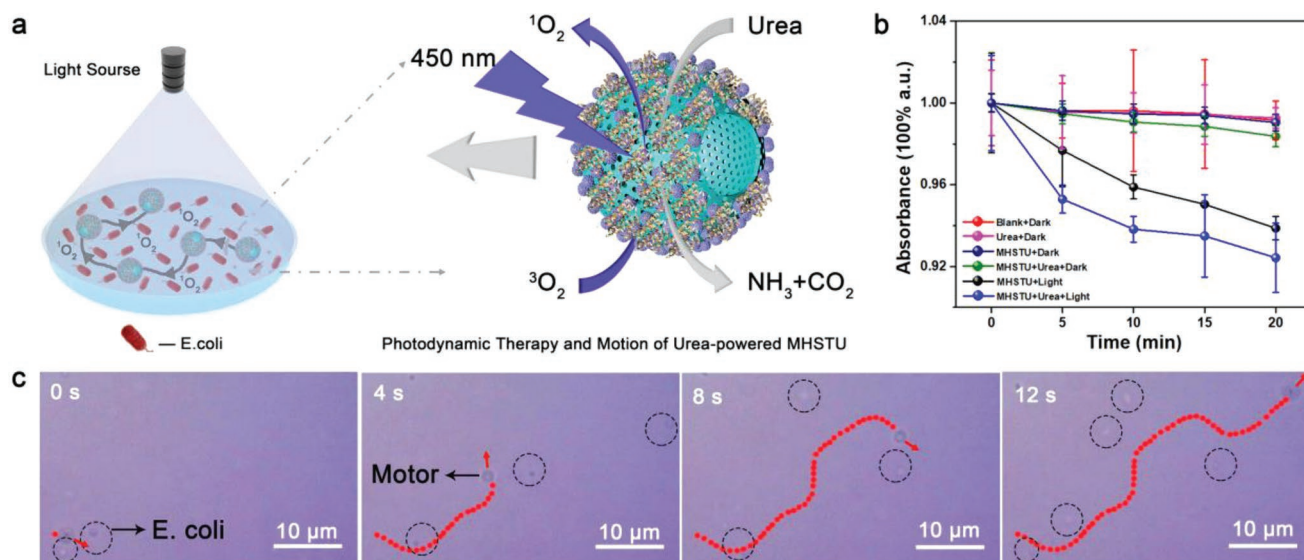
Figure 4. a) Schematic illustration showing the mobile MHSTU platform for PDT against *E. coli* under blue light irradiation in vitro. b) The variation trend of the peak values at 378 nm of UV–vis spectra of ABDA with samples within 20 min, including MHSTU under irradiation, MHSTU and Urea under irradiation, DI water, Urea, MHSTU without irradiation, and MHSTU and Urea without irradiation. (Error bars indicate standard deviation, *N* = 4). c) Video snapshots of a typical moving MHSTU in a solution containing 25 mmol L^{-1} urea and living *E. coli*.
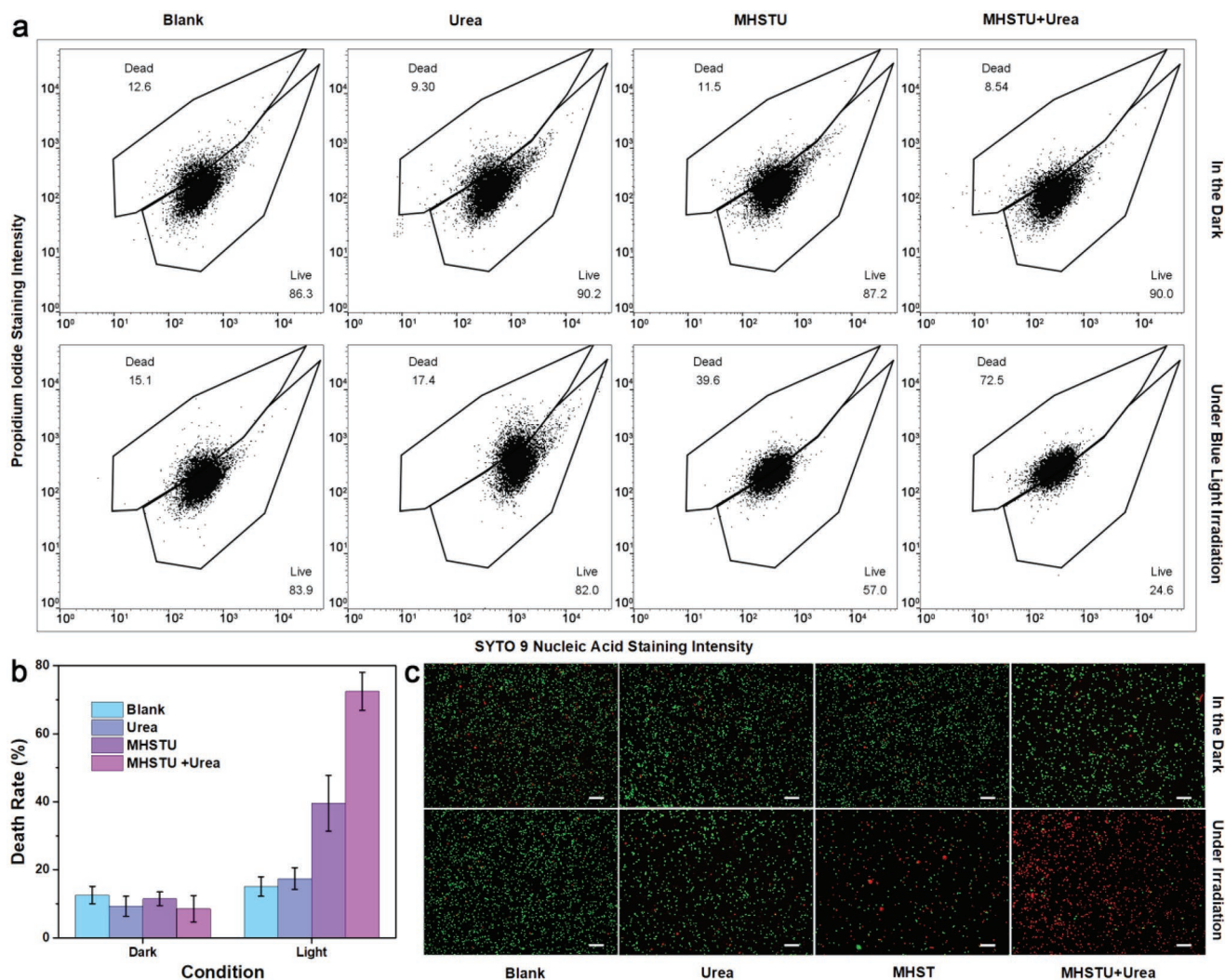
Figure 5. a) The viability of *E. coli* after different treatments determined by flow cytometry. b) The plot showing the death rates of *E. coli* after different treatments. Error bars indicate standard deviation, $N = 4$. c) Merged images of the dead *E. coli* (red) and the live *E. coli* (green) after different treatments, respectively. Scale bar = 25 µm.

Figure 4c. As for MHSTU and *E. coli* in 25 mmol L^{-1} urea solution, MHSTU was fueled by urea and actively moved around the solution, while *E. coli* still performed Brownian motion within a very small local area. That is to say, the MHSTU as a mobile photosensitizer platform could actively travel around within the solution to spread $^1O_2$ and approach much more *E. coli* compared to conventional passive photosensitizer nanocarriers, promising highly efficient PDT antimicrobial activity.

2.5. Enhanced PDT Effect against Bacteria

The flow cytometry assay and fluorescence microscopy observation were carried out to evaluate the PDT effect against bacteria using LIVE/DEAD BacLight Bacterial Viability and Counting Kit.[38] The living *E. coli* can be labeled by SYTO 9 nucleus acid staining with green fluorescence emission and the dead *E. coli* can be labeled by propidium iodide staining with red fluorescence emission. Details about the PDT experiment are provided in the Experimental Section. The death rates of *E. coli* after different treatments were analyzed by flow cytometry as shown in **Figure 5**a and the corresponding results are presented in Figure 5b and Table S1 in the Supporting Information. In addition, the merged fluorescence images with both green (living bacteria) and red (dead bacteria) channels of *E. coli* after different treatments are shown in Figure 5c. The results from fluorescent microscopy observation are approximately consistent with the dead rates provided in Figure 5b. For the negative control groups without light irradiation (upper column in Figure 5a), including *E. coli* treated with DI water, urea (25 mmol L^{-1}), MHSTU (100 µg mL^{-1}), and both MHSTU (100 µg mL^{-1}) and urea (25 mmol L^{-1}), the majority (almost 90%) of the bacteria are located in lower bracket area where the bacteria were stained with green fluorescent emission and assumed to be alive. The corresponding fluorescent images in Figure 5c also support this result which indicates that urea, MHSTU, and

**ADVANCED
SCIENCE NEWS**
www.advancedsciencenews.com

**ADVANCED
FUNCTIONAL
MATERIALS**
www.afm-journal.de

the mixture of MHSTU and urea have little cytotoxicity toward *E. coli* (Figure 5a). The *E. coli* treated with 450 nm light irradiation (14.2 mW cm^{-2}) only with or without urea also showed very low death rate as well, 15.1% and 17.4% respectively, suggesting that either the used blue light or the urea has negligible effect on the viability of *E. coli*. However, the death rate of *E. coli* treated with MHSTU under blue light irradiation increased to 39.6%, showing notable photodynamic cytotoxicity against *E. coli*, indicating that MHSTU generated cytotoxic $^1O_2$ which killed *E. coli* efficiently. And the death rate of *E. coli* treated with MHSTU when fueled with urea under blue light irradiation is as high as 72.5%. The significant enhancement of the PDT effect can be probably explained by two main reasons. First, the available $^3O_2$ surrounding MHSTU is limited and the passive MHSTU cannot make full use of the photodynamic capability of TAPP, however the urea-driven MHSTU can actively move and get access to more $^3O_2$. Second, the diffusion range of $^1O_2$ was reported to be within 200 nm in physiological condition due to its short lifetime,[11] which means only the bacteria next to MHSTU can be killed. However, the self-propelled motors can "on-the-fly" generate and spread $^1O_2$ around by active propulsion, resulting in much higher possibility of bacteria killing. In addition, in the course of our experiment, we found that many of the MHSTU motors moved within 3D solution rather than only on planar surfaces, since the motors moving in 3D easily went out of focus during the video tracking (Video S6, Supporting Information). This is possibly due to the hollow structure induced slow sedimentation and its active propulsion that reorients its body. The capability of actively moving in 3D not only implies that the urea-driven MHSTU can efficiently interact with *E. coli* in 3D suspension, but also suggests that this enzymatic micromotor based mobile PDT strategy holds potential for practical disinfection application in 3D scenario. Therefore, we have successfully demonstrated a highly efficient PDT process by using the enzymatically propelled mobile photosensitizer platform.

3. Conclusion

In summary, we have designed and fabricated a multifunctionalized micromotor as a mobile photosensitizer platform. Instead of constructing Janus structures, the MHSTU with the intrinsic asymmetry formed by one-step chemical reaction can perform active motion powered by biocompatible fuel of urea, which can facilitate future massive production by bulk solution synthesis. The propulsion mechanism of the urea-driven MHSTU was verified by numerical modeling, and we clarified the movement direction of the micromotor against the hole on the surface of the MHSTU. Magnetotaxis transportation of the micromotors can be accomplished by the external magnetic field for targeted on-chip PDT. Compared to passive carriers under the same condition, the single oxygen generation capability of the mobile photosensitizer was enhanced by more than 20% and the active motion can significantly enlarge the coverage area of the MHSTU by about 10 times to spread $^1O_2$, which results in highly efficient photodynamic activity. The enhanced PDT effect was confirmed by the targeted on-chip

PDT process against *E. coli* via flow cytometry assay and fluorescence microscopy observation.

Overall, such a platform not only promotes the development of the fabrication and functionalization of MNMs, but also provides new perspectives for the synergy between the field of MNMs and PDT for further biomedical application. Limitations still exist, such as a much-decreased activity of MHSTU micromotors in solutions of high ionic strength, that hinder the direct application of this platform in vivo. However, a number of research groups worldwide are actively seeking solutions to this issue of ionic strength, and breakthroughs in this front could enable the rapid transfer of the current technology. Until then, MHSTU with PDT capability could potentially find uses in treating bacterial infections in vitro and even antitumor applications in vivo.

4. Experimental Section

Materials and Characterization: Polyvinylpyrrolidone (K-30, >98%), styrene, 2,2′-azo-bis(isobutyronitrile) (AIBN, 98%), isopropanol (IPA), cetyltrimethylammonoium bromide (CTAB, 99%), ammonia (NH$_3$·H$_2$O, 25%), tetraethylorthosilicate (TEOS, 99%), 3-aminopropyltriethoxysilane (APTES, 99%), ethanol (EtOH, >99%), dimethylformamide (DMF, >99%), PBS (pH = 7.0-7.2), sodium citrate (Na$_3$C$_6$H$_5$O$_7$·2H$_2$O), sodium hydroxide (NaOH), sodium nitrate (NaNO$_3$), ferrous sulfate (FeSO$_4$·7H$_2$O), *N*-(3-dimethylaminopropyl)-*N*′-ethylcarbodiimide hydrochloride (EDC), *N*-hydroxysuccinimide (NHS, 98%), 5,10,15,20-tetrakis(4-aminophenyl) porphyrin (>95.0%), glutaraldehyde (50%), Jack bean urease from Canavalia ensiformis (Type IX, powder, 50000-100000 unites g^{-1} solid), tryptone, yeast extract, sodium chloride (NaCl, ≥99.5%), sodium hydroxide (NaOH, ≥96.0%), 9,10-anthracenediyl-bis-(methylene) dimalonic acid, and LIVE/DEAD BacLight Bacterial Viability and Counting Kit for flow cytometry were purchased commercially and used as-received. SEM images and energy dispersive X-ray (EDX) spectroscopy were captured by Carl Zeiss Microscopy GmbH GeminiSEM 300 and Oxford instruments X-Max, respectively. The size distribution and zeta potential were characterized by dynamic light scattering (DLS) with Zetasizer Nano ZS90. FT-IR spectra were analyzed by a Fourier-transformed infrared spectrometer (Nicolet380, Thermo). UV–vis adsorption spectra were measured by a spectrometer (UV-3600, Shimadzu). Fluorescence spectra were characterized by a spectrofluorimeter (RF 5301, Thermo). Optical videos and fluorescence images were taken by a Leica inverted optical microscope (Leica DMi8) with a 40× air objective. Flow cytometry data were obtained via CyFlow Cube 6 (Sysmex Partec).

Preparation of Polystyrene Microparticles: A typical preparation of polystyrene with some modifications is as follows.[39] First, K-30 (0.25 g) was dissolved in a mixture of IPA (45 mL) and deionized water (5 mL). Then styrene (10 g) and AIBN (0.17 g) were added into the mixture, which was heated to 70 °C and kept stirring under nitrogen gas flux for 24 h. The obtained polystyrene particles were washed with a mixture ethanol and DI water at the volume ratio of 1:1 for five times and finally suspended in ethanol for further use.

Preparation of Amine-Modified Hollow mSiO$_2$ (HS-NH$_2$): HS-NH$_2$ was prepared according to a previous report with some modifications.[28] Polystyrene (50 mg), CTAB (10 mg), and NH$_3$·H$_2$O (50 µL) were added into the mixture solution of DI water (1.3 mL) and ethanol (1 mL), which was sonicated for 5 min. Then, TEOS (17.5 µL) was added into the mixture under continuous stirring. After reacting for 6 h, APTES (3 µL) was added. The new mixture was kept stirring for another 16 h. The polystyrene encapsulated with mesoporous silica particles, named as polystyrene@mSiO$_2$-NH$_2$, were collected and washed with ethanol twice. Then, the removal of the polystyrene template was realized by washing with DMF five times to form HS-NH$_2$. After being washed with

the mixture of ethanol and DI water three times, the HS-NH$_2$ particles were dispersed in DI water for further use.

Preparation of Fe$_3$O$_4$ Nanoparticles: Fe$_3$O$_4$ was synthesized by a previously reported method.[29] Briefly, sodium citrate (29.41 mg), NaOH (160 mg), and NaNO$_3$ (17 g) were dissolved in DI water (19 mL). FeSO$_4$·7H$_2$O solution (2 mol L^{-1}, 1 mL) was rapidly added into the abovementioned mixture. Then, the mixture became transparent and was heated to 100 °C. The new mixture was kept mechanical agitation at 100 °C for 1 h, and then cooled to room temperature naturally. The Fe$_3$O$_4$ nanoparticles were obtained after being washed and purified several times by magnetic separation, which were dispersed in DI water for further use.

Preparation of Magnetic HS-TAPP (MHST): EDC (5 mg) and HS-NH$_2$ (5 mg) were added into TAPP PBS solution (1 mg mL^{-1}, 5 mL), which was strongly shaken for 1 h. NHS (3 mg) and Fe$_3$O$_4$ (5 mg) were then added into the abovementioned solution under continuous shaking for another 3 h. MHST was obtained after centrifugation and washing with PBS at low rotation rate several times to remove the impurity.

Preparation of MHST-Urease (MHSTU): MHSTU was prepared by a method reported previously.[28] Typically, MHST (5 mg) obtained in the previous step were suspended in PBS (1 mL) containing of GA (50 μL), which was used as a linker molecule. The mixture solution was kept shaking for 3 h. The GA activated MHST particles were washed with PBS five times and then resuspended in PBS (1 mL) containing urease (3 mg). The new mixture was gently shaken at room temperature for 12 h. MHSTU was obtained after washing with DI water five times. Finally, the products were suspended in DI water and stored at 4 °C for further use.

Optical Video Recording: Leica DMi8 with a 40× objective was utilized to study the movement of the motors. The MHSTU solution (10 μL) with proper concentration and urea solution (10 μL) with varying concentrations were placed in a 0.8 mm high Petri dish and covered with a coverslip to minimize the drifting effect. The concentration of urea solution was 0, 10, 25, 50, and 100 mmol L^{-1}, respectively. By the same strategy, the movement behavior of enzymatic powered MHSTU was studied in 25 mmol L^{-1} urea solution with 0.005, 0.05, 0.5, 5, and 50 mmol L^{-1} saline (NaCl). In addition, a self-built 2D magnetic control platform was utilized to manipulate the directional movement and swarming behavior of the motors. The current and voltage applied were 1.0 A and 32 V, and the strength of the generated magnetic field was about 10 mT. The videos of the movement condition of motors were recorded via a CCD camera at the frame rate of about 30 fps.

COMSOL Simulation:

1) Assumptions of chemical species and flux

On motor surface, urea converts into NH$_3$ and CO$_2$ by urease following

$$CO(NH_2)_2 + H_2O = 2NH_3 + CO_2 \tag{1}$$

Since a urease molecule had 3 catalytic sites, and the turnover rate for each site was 5913,[40] the maximum reaction rate for urea conversion can be calculated to be V_{max} = 17 739 molecules of urea per second per molecule of urease. The dimeter of one urease molecule is roughly 10 nm, and one urease molecule occupies a square area s of 10 × 10 nm^2. It is assumed that urease molecules attach to motor outer surface uniformly and are close packed. The flux, defined as the number of moles of chemical species per unit area per second, is therefore calculated by

$$J = \frac{V_{max}}{N_A s} \tag{2}$$

where J is the flux, V_{max} is the maximum reaction rate for each enzyme molecule, N_A is Avogadro constant, and s is the area of each enzyme molecule. The flux of NH$_3$ is calculated to be 5.89×10^{-4} mol m^{-2} s^{-1}, and the flux of CO$_2$ is 2.94×10^{-4} mol m^{-2} s^{-1}. Since both NH$_3$ and

CO$_2$ are produced by the enzymatic reaction, they reach a chemical equilibrium that contain many chemical species in the solution. To simplify this model, it was assumed that at the initial stage of motor motion the solution was saturated with atmospheric CO$_2$ and the pH value was ≈5.6. At such a condition, the produced NH$_3$ molecules almost completely dissociate into NH$_4^+$ and OH$^-$ via the following equation with a K_b of 1.78×10^{-5}

$$NH_3 \cdot H_2O \leftrightarrow NH_4^+ + OH^- \tag{3}$$

Although as time progresses the solution pH will increase, at the beginning the dissolution of CO$_2$ and its dissociation at a roughly neutral pH can be ignored compared to that of NH$_3$. In this model, therefore only the diffusion of NH$_4^+$ and OH$^-$ ions near motor surface was considered, with a flux of 5.89×10^{-4} mol m^{-2} s^{-1} for both ions.

2) Model implementation

Based on the previous works,[41] a thin double layer assumption was used and fluxes near the surface were only in the direction vertical to the surface. Ion fluxes due to convention were neglected because of its relatively small contribution. A 2D axisymmetric model was used in COMSOL Multiphysics package (version 5.2a). As is shown in Figure S8a in the Supporting Information, the length of the box is 100 μm, the outer dimeters of hollow SiO$_2$ sphere is 2 μm, and the internal dimeter is 1.8 μm. The dimeter of hole is typically 0.5 μm as shown in Figure S8b in the Supporting Information. Electrostatics and creeping flow modules were used in COMSOL model. In the electrostatics module, the outer surface of hollow sphere produced an ions flux of NH$_4^+$ and OH$^-$ and also carried an extrinsic surface charge density that was related to flux (flux_outside) and the diffusivities of NH$_4^+$ ($D_{NH_4^+}$) and OH$^-$ (D_{OH^-}) by

$$\rho = \varepsilon E = \varepsilon \frac{J k_B T}{2 e n_0} \left(\frac{1}{D_{NH_4^+}} - \frac{1}{D_{OH^-}} \right) \tag{4}$$

where ε is the medium electrical permittivity and n_0 is the bulk ion concentration. The starting pH of the solution was considered to be close to 5.65 of water saturated with CO$_2$, so the bulk concentration of protons and bicarbonate ion can be calculated to be 2.24×10^{-6} mol L^{-1}. In creeping flow module, there was an electro-osmotic boundary condition applied to both the internal and outer surface

$$v = \frac{\zeta \varepsilon}{\mu} E \tag{5}$$

where v is the electro-osmotic speed of fluid at motor surface, ζ is the zeta potential of outer surface or internal surface, μ is the dynamic viscosity of water, and E is the tangential component of the electric field. The top and bottom of the box were set to be open boundary for the flow, and the side walls were completely slip boundaries (no stress). Parameters used in COMSOL simulation are shown in Table S2 in the Supporting Information. Further notes about this simulation are provided in the Supporting Information.

Mean-Square-Displacement and Coverage Area Analysis: The tracking trajectory of the motors was carried out by Image J, a public image processing software. After the tracking trajectory of the motors were obtained, MSD was analyzed according to the following formula, $MSD(\Delta t) = [(x_i(t + \Delta t) - x_i(t))^2]$ ($i = 2$, for 2D analysis), via a self-developed code based on Python. The coverage area was calculated by the trajectory length within 15 s and the average radius of the motors. Under different conditions, 15 motors were analyzed to obtain statistics.

Detection of $^1O_2$ Generation Capability of Samples: MHSTU (100 μg), urea aqueous solution (50 mmol L^{-1}, 100 μL), and saturated ABDA aqueous solution (100 μL) were mixed together. The absorption spectra of the mixture was measured after the mixture was irradiated by a laser source (FU450289MTX100-GD16, 450 nm) and kept in the dark for 0, 5, 10, 15, and 20 min, respectively.[8] Similarly, controlled trials were also carried out to saturated ABDA aqueous solution (100 μL) mixed with

MHSTU aqueous solution (1 mg mL⁻¹, 100 µL). DI water (100 µL) and urea aqueous solution (50 mmol L⁻¹, 100 µL) mixed with saturated ABDA were kept in the dark for 0, 5, 10, 15, and 20 min as controls, respectively. The power of the light source applied was about 3.9 mW cm⁻².

Bacteria Culture: Bacteria culture medium was self-made for bacteria culture. First, tryptone (10 g), yeast extract (5 g), and NaCl (10 g) were dissolved in DI water. The pH value of the mixture was stabilized at around 7.4 after being regulated with NaOH. Then, the mixture solution was diluted with DI water to 1 L and the bacteria culture medium was obtained. Finally, the bacteria culture medium was divided into two dozen sealed centrifuge tubes. All bacteria culture medium were sterilized before use. *E. coli* was cultured with bacterial culture medium in an oscillating incubator at 37 °C.

Bacteria Staining and Flow Cytometry Assay: LIVE/DEAD BacLight Bacterial Viability and Counting Kit for flow cytometry was used for bacteria staining and flow cytometry assay, which utilizes a mixture of two nucleic acid stains, including green-fluorescent SYTO 9 dye (for the live) and red-fluorescent propidium iodide dye (for the dead), for viability determinations.[38] *E. coli* was washed with DI water three times and suspended in DI water (2 mL), which was seeded into two 35 mm culture dishes. Then, the mixture (2 mL) containing MHSTU (200 µg mL⁻¹) and urea (50 mmol L⁻¹) was respectively added into two dishes, in which the height of the mixture was around 2 mm. One dish was treated in the dark for 15 min, and the other was exposed to the blue light for 15 min. After being incubated for 1 h, *E. coli* was collected from the two dishes, respectively, and washed by centrifugation or magnetic separation, then resuspended in DI water in two tubes. SYTO 9 (1.5 µL) and propidium iodide (1.5 µL) were dispersed into each tube, respectively, which were kept in the dark for 15 min for bacteria staining. The stained *E. coli* was used for both fluorescent image capture and flow cytometry assay. Similarly, *E. coli* was also treated with DI water, urea (50 mmol L⁻¹), and MHSTU (200 µg mL⁻¹) as controls. The power of the light source applied was about 14.2 mW cm⁻².

Supporting Information

Supporting Information is available from the Wiley Online Library or from the author.

Conflict of Interest

The authors declare no conflict of interest.

[1] a) D. E. J. G. J. Dolmans, D. Fukumura, R. K. Jain, *Nat. Rev. Cancer* **2003**, *3*, 380; b) P. Agostinis, K. Berg, K. A. Cengel, T. H. Foster, A. W. Girotti, S. O. Gollnick, S. M. Hahn, M. R. Hamblin, A. Juzeniene, D. Kessel, M. Korbelik, J. Moan, P. Mroz, D. Nowis, J. Piette, B. C. Wilson, J. Golab, *Ca-Cancer J. Clin.* **2011**, *61*, 250; c) A. Tavares, C. M. B. Carvalho, M. A. Faustino, M. G. P. M. S. Neves, J. P. C. Tomé, A. C. Tomé, J. A. S. Cavaleiro, Â. Cunha, N. C. M. Gomes, E. Alves, A. Almeida, *Mar. Drugs* **2010**, *8*, 91; d) T. Dai, Y. Huang, M. R. Hamblin, *Photodiagn. Photodyn. Ther.* **2009**, *6*, 170.

[2] a) B. W. Henderson, T. J. Dougherty, *Photochem. Photobiol.* **1992**, *55*, 145; b) Á. Juarranz, P. Jaén, F. S. Rodríguez, J. Cuevas, S. González, *Clin. Transl. Oncol.* **2008**, *10*, 148.

[3] a) B. W. Henderson, V. H. Fingar, *Cancer Res.* **1987**, *47*, 3110; b) T. H. Foster, R. S. Murant, R. G. Bryant, R. S. Knox, S. L. Gibson, R. Hilf, *Radiat. Res.* **1991**, *126*, 296; c) S. Hatz, L. Poulsen, P. R. Ogilby, *Photochem. Photobiol.* **2008**, *84*, 1284.

[4] J. Moan, *J. Photochem. Photobiol., B* **1990**, *6*, 343.

[5] a) R. Bonnett, *Chem. Soc. Rev.* **1995**, *24*, 19; b) K. Kano, K. Fukuda, H. Wakami, R. Nishiyabu, R. F. Pasternack, *J. Am. Chem. Soc.* **2000**, *122*, 7494; c) D. Gabrielli, E. Belisle, D. Severino, A. J. Kowaltowski, M. S. Baptista, *Photochem. Photobiol.* **2007**, *79*, 227.

[6] a) X. Ma, S. Sreejith, Y. Zhao, *ACS Appl. Mater. Interfaces* **2013**, *5*, 12860; b) X. Qiao, J. Zhou, J. Xiao, Y. Wang, L. Sun, C. Yan, *Nanoscale* **2012**, *4*, 4611.

[7] M. Lismont, L. Dreesen, S. Wuttke, *Adv. Funct. Mater.* **2017**, *27*, 1606314.

[8] D. Xu, Y. You, F. Zeng, Y. Wang, C. Liang, H. Feng, X. Ma, *ACS Appl. Mater. Interfaces* **2018**, *10*, 15517.

[9] a) W. Fan, W. Bu, B. Shen, Q. He, Z. Cui, Y. Liu, X. Zheng, K. Zhao, J. Shi, *Adv. Mater.* **2015**, *27*, 4155; b) C. Zhang, K. Zhao, W. Bu, D. Ni, Y. Liu, J. Feng, J. Shi, *Angew. Chem., Int. Ed.* **2015**, *54*, 1770.

[10] S. S. Lucky, K. C. Soo, Y. Zhang, *Chem. Rev.* **2015**, *115*, 1990.

[11] E. Skovsen, J. W. Snyder, J. D. C. Lambert, P. R. Ogilby, *J. Phys. Chem. B* **2005**, *109*, 8570.

[12] a) M. Safdar, S. U. Khan, J. Janis, *Adv. Mater.* **2018**, *30*, e1703660; b) B. Xu, B. Zhang, L. Wang, G. Huang, Y. Mei, *Adv. Funct. Mater.* **2018**, *28*, 1705872; c) L. Xu, F. Mou, H. Gong, M. Luo, J. Guan, *Chem. Soc. Rev.* **2017**, *46*, 6905; d) J. Katuri, X. Ma, M. M. Stanton, S. Sanchez, *Acc. Chem. Res.* **2017**, *50*, 2; e) W. Gao, J. Wang, *ACS Nano* **2014**, *8*, 3170.

[13] M. Cianchetti, C. Laschi, A. Menciassi, P. Dario, *Nat. Rev. Mater.* **2018**, *3*, 143.

[14] J. Li, B. Esteban-Fernandez de Ávila, W. Gao, L. Zhang, J. Wang, *Sci. Rob.* **2017**, *2*, eaam6431.

[15] a) M. Medina-Sánchez, H. Xu, O. G. Schmidt, *Ther. Delivery* **2018**, *9*, 303; b) M. Luo, Y. Feng, T. Wang, J. Guan, *Adv. Funct. Mater.* **2018**, *28*, 1706100.

[16] B. E. de Ávila, P. Angsantikul, J. Li, M. Angel Lopez-Ramirez, D. E. Ramirez-Herrera, S. Thamphiwatana, C. Chen, J. Delezuk, R. Samakapiruk, V. Ramez, M. Obonyo, L. Zhang, J. Wang, *Nat. Commun.* **2017**, *8*, 272.

[17] J. Guo, J. J. Gallegos, A. R. Tom, D. Fan, *ACS Nano* **2018**, *12*, 1179.

[18] B. Esteban-Fernandez de Ávila, D. E. Ramirez-Herrera, S. Campuzano, P. Angsantikul, L. Zhang, J. Wang, *ACS Nano* **2017**, *11*, 5367.

[19] a) X. Xu, S. Hou, N. Wattanatorn, F. Wang, Q. Yang, C. Zhao, X. Yu, H. R. Tseng, S. J. Jonas, P. S. Weiss, *ACS Nano* **2018**, *12*, 4503; b) F. Qiu, S. Fujita, R. Mhanna, L. Zhang, B. R. Simona, B. J. Nelson, *Adv. Funct. Mater.* **2015**, *25*, 1666.

[20] Y. Tu, F. Peng, A. A. Andre, Y. Men, M. Srinivas, D. A. Wilson, *ACS Nano* **2017**, *11*, 1957.

[21] Z. Wu, B. Esteban-Fernandez de Ávila, A. Martin, C. Christianson, W. Gao, S. K. Thamphiwatana, A. Escarpa, Q. He, L. Zhang, J. Wang, *Nanoscale* **2015**, *7*, 13680.

[22] L. K. Abdelmohsen, M. Nijemeisland, G. M. Pawar, G. J. Janssen, R. J. Nolte, J. C. van Hest, D. A. Wilson, *ACS Nano* **2016**, *10*, 2652.

[23] a) H. Xu, M. Medina-Sanchez, V. Magdanz, L. Schwarz, F. Hebenstreit, O. G. Schmidt, *ACS Nano* **2018**, *12*, 327; b) R. Mhanna, F. Qiu, L. Zhang, Y. Ding, K. Sugihara, M. Zenobi-Wong, B. J. Nelson, *Small* **2014**, *10*, 1953.

[24] X. Ma, K. Hahn, S. Sanchez, *J. Am. Chem. Soc.* **2015**, *137*, 4976.

[25] a) J. Orozco, A. Cortes, G. Cheng, S. Sattayasamitsathit, W. Gao, X. Feng, Y. Shen, J. Wang, *J. Am. Chem. Soc.* **2013**, *135*, 5336; b) M. Hansen-Bruhn, B. E. de Avila, M. Beltran-Gastelum, J. Zhao, D. E. Ramirez-Herrera, P. Angsantikul, K. Vesterager Gothelf, L. Zhang, J. Wang, *Angew. Chem., Int. Ed.* **2018**, *57*, 2657.

[26] T. Y. Ohulchanskyy, I. Roy, L. N. Goswami, Y. Chen, E. J. Bergey, R. K. Pandey, A. R. Oseroff, P. N. Prasad, *Nano Lett.* **2007**, *7*, 2835.

[27] a) F. Ricchelli, *J. Photochem. Photobiol., B* **1995**, *29*, 109; b) R. W. Boyle, D. Dolphin, *Photochem. Photobiol.* **1996**, *64*, 469.

[28] X. Ma, X. Wang, K. Hahn, S. Sanchez, *ACS Nano* **2016**, *10*, 3597.

[29] C. Hui, C. Shen, T. Yang, L. Bao, J. Tian, H. Ding, C. Li, H. J. Gao, *J. Phys. Chem. C* **2008**, *112*, 11336.

[30] M. Shaik, I. A. Motaleb, presented at *IEEE Int. Conf. on Electro-Information Technology*, Rapid City, USA, May **2013**.

[31] M. Mandal, S. Kundu, S. K. Ghosh, S. Panigrahi, T. K. Sau, S. M. Yusuf, T. Pal, *J. Colloid Interface Sci.* **2005**, *286*, 187.

[32] a) E. V. Savinkina, D. V. Golubev, M. S. Grigoriev, *J. Coord. Chem.* **2011**, *64*, 3758; b) E. Podstawka, M. Światłowska, E. Borowiec, L. M. Proniewicz, *J. Raman Spectrosc.* **2007**, *38*, 356.

[33] A. M. Pourrahimi, M. Pumera, *Nanoscale* **2018**, *10*, 16398.

[34] T. Patiño, X. Arqué, R. Mestre, L. Palacios, S. Sánchez, *Acc. Chem. Res.* **2018**, *51*, 2662.

[35] T. Patiño, N. Feiner-Gracia, X. Arqué, A. Miguel-López, A. Jannasch, T. Stumpp, E. Schäffer, L. Albertazzi, S. Sánchez, *J. Am. Chem. Soc.* **2018**, *140*, 7896.

[36] a) K. V. Rajagopalan, I. Fridovich, P. Handler, *J. Biol. Chem.* **1961**, *236*, 1059; b) G. B. Kistiakowsky, A. J. Rosenberg, *J. Am. Chem. Soc.* **1952**, *74*, 5020.

[37] a) F. Peng, Y. Tu, Y. Men, J. C. van Hest, D. A. Wilson, *Adv. Mater.* **2017**, *29*, 1604996; b) T. Li, X. Chang, Z. Wu, J. Li, G. Shao, X. Deng, J. Qiu, B. Guo, G. Zhang, Q. He, L. Li, J. Wang, *ACS Nano* **2017**, *11*, 9268.

[38] a) N. Chimnoi, N. Reuk-ngam, P. Chuysinuan, P. Khlaychan, N. Khunnawutmanotham, D. Chokchaichamnankit, W. Thamniyom, S. Klayraung, C. Mahidol, S. Techasakul, *Microb. Pathog.* **2018**, *118*, 290; b) J. He, J. Chen, G. Hu, L. Wang, J. Zheng, J. Zhan, Y. Zhu, C. Zhong, X. Shi, S. Liu, Y. Wang, L. Ren, *J. Mater. Chem. B* **2018**, *6*, 68.

[39] G. Qi, Y. Wang, L. Estevez, A. K. Switzer, X. Duan, X. Yang, E. P. Giannelis, *Chem. Mater.* **2010**, *22*, 2693.

[40] B. Krajewska, *J. Mol. Catal. B: Enzym.* **2009**, *59*, 9.

[41] a) C. Liu, C. Zhou, W. Wang, H. Zhang, *Phys. Rev. Lett.* **2016**, *117*, 198001; b) T. Y. Chiang, D. Velegol, *Langmuir* **2014**, *30*, 2600; c) T. R. Kline, J. Iwata, P. E. Lammert, T. E. Mallouk, A. Sen, D. Velegol, *J. Phys. Chem. B* **2006**, *110*, 24513.

1807727 (11 of 11)